1   **Modeling groundwater responses to climate change in the Prairie Pothole Region**

6   Zhe Zhang[1], Yanping Li[1*], Michael Barlage[2], Fei Chen[2], Gonzalo Miguez-Macho[3], Andrew Ireson[1],

7   Zhenhua Li[1]

9   [1]*Global Institute for Water Security, University of Saskatchewan, Saskatoon, SK, Canada*

10   [2]*National Center for Atmospheric Research, Boulder, Colorado, USA*

11   [3]*Nonlinear Physic Group, Faculty of Physics, Universidade de Santiago de Compostela, Galicia, Spain*

13   Abstract

14   Shallow groundwater in the Prairie Pothole Region (PPR) is recharged predominantly by snowmelt

15   in the spring and supplies water for evapotranspiration through the summer and fall. This two-way

16   exchange is underrepresented in current land surface models. Furthermore, the impacts of climate

17   change on the groundwater recharge rates are uncertain. In this paper, we use a coupled land and

18   groundwater model to investigate the hydrological cycle of shallow groundwater in the PPR and

19   study its response to climate change at the end of the 21st century. The results show that the model

20   does a reasonably good job of simulating the timing of recharge. The mean water table depth

21   (WTD) is well simulated, except the model predicts deep WTD in northwestern Alberta. The most

22   significant change under future climate conditions occurs in the winter, when warmer temperature

23   changes the rain/snow partitioning, delaying the time for snow accumulation/soil freezing while

24   advancing early melting/thawing. Such changes lead to an earlier start to a longer recharge season,

25   but with lower recharge rates. Different signals are shown in the eastern and western PPR in the

26   future summer, with reduced precipitation and drier soils in the east but little change in the west.

27   The annual recharge increased by 25% and 50% in the eastern and western PPR, respectively.

28   Additionally, we found the mean and seasonal variation of the simulated WTD are sensitive to

29   soil properties and fine-scale soil information is needed to improve groundwater simulation on

30   regional scale.

32   Keywords: Groundwater, Recharge, Climate Change, Prairie Pothole Region, Hydrological Cycle,

Introduction

The Prairie Pothole Region (PPR) in North America is located in a semi-arid and cold region, where evapotranspiration (ET) exceeds precipitation (PR) in summer and near-surface soil is frozen in winter (Gray, 1970; Granger and Gray, 1989; Hayashi et al., 2003; Pomeroy et al., 2007; Ireson et al., 2013; Dumanski et al., 2015). These climatic conditions have introduced unique hydrological characters to the groundwater flow in the PPR (Ireson et al., 2013). During winters, frozen soils reduce permeability and snow accumulates on the surface, prohibiting infiltration (Niu and Yang 2006; Mohammed et al., 2018). At the same time, the water table slowly declines due to a combination of upward transport to the freezing front by the capillary effect and discharge to rivers (Ireson et al., 2013). In early spring, snowmelt becomes the dominant component of the hydrological cycle and the melt water runs over frozen soil, with little infiltration contributing to recharge. As the soil thaws, the increased infiltration capacity allows snowmelt recharge to the water table, the previously upward water movement by capillary effect to reverse and move downwards, and the water table to rise to its maximum level. In summer and fall, when high ET exceeds PR, capillary rise may draw water from the groundwater aquifers to supply ET demands, declining water table. These processes characterize the two-way water exchange between sub-surface soils and groundwater aquifers.

Previous studies have suggested that substantial changes to groundwater interactions with sub-surface soils are likely to occur under climate change (Tremblay et al., 2011; Green et al., 2011; Ireson et al., 2013, 2015). Existing modeling studies on the impacts of climate change on groundwater are either at global or basin/location-specific scales (Meixner et al., 2016). Global-level groundwater studies focus on potential future recharge trends (Doll and Fiedler, 2008; Doll,

56   2009; Green et al., 2011), yet coarse resolution analysis from global climate models (GCMs)

57   provided insufficient specificity to inform decision making. Basin-scale groundwater studies

58   connect the climate with groundwater-flow models to understand the climate impacts on specific

59   systems (Maxwell and Kollet, 2008; Kurylyk and MacQuarrie, 2013; Dumanski et al., 2015).

60   Regional groundwater modeling studies, such as in the Colorado River Basin (Christensen et al.,

61   2004) and in the western U.S. (Niraula et al., 2017), have applied downscaled climate scenarios

62   from GCMs to drive large scale hydrology models. These studies identified research gaps

63   associated with poor representation of groundwater-soil interactions in models and uncertainties

64   in future climate projections.

65

66   It is challenging to represent groundwater flows in LSMs because the important two-way water

67   exchange between unsaturated soils and groundwater aquifers was neglected in previous LSMs.

68   Recently, this two-way exchange has been implemented in coupled land surface – groundwater

69   models (LSM-GW). For example, Maxwell and Miller (2005) used a groundwater model (ParFlow)

70   coupled with the Common Land Model (CLM) as a single column model. They found that the

71   coupled and uncoupled models were very similar in simulated sensible heat flux (SH), ET, and

72   shallow soil moisture (SM), but differed greatly in simulated runoff and deep SM. Later on, Kollet

73   and Maxwell (2008) incorporated the ET effect on redistributing moisture upward from shallow

74   water table depth (WTD) and found the surface energy partitioning is highly sensitive to the WTD

75   when the WTD is less than 5 m below ground surface. Niu et al. (2011) implemented a simple

76   groundwater model (SIMGM, Niu et al., 2007), into the community Noah LSM with multi-

77   parameterization options (Noah-MP LSM), by adding an unconfined aquifer at the bottom of soil

78   layers. More complex features such as three-dimensional subsurface flow and two-dimensional

79   surface were included in ParFlow v3 and evaluated over much of continental North America for a

80   very fine 1-km resolution (Maxwell et al., 2015). These recent development in coupled land and

81   groundwater models have advanced our knowledge on the important interactions between soil and

82   groundwater aquifer.

83

84   In cold regions, soil freeze-thaw processes further complicate this two-way exchange. Field studies

85   have found that frozen soil not only influences the timing and amount of downward recharge to

86   aquifers by reducing the soil permeability (Koren et al., 1999; Niu et al., 2006; Kelln et al., 2007),

87   but may also induce upward water transport from aquifers to soil freezing fronts (Spaans and Baker,

88   1996; Remenda et al., 1996; Hansson et al., 2004). In the modeling community, a range of

89   approaches have been applied to deal with frozen soil parameterizations. Earlier LSMs assumed

90   no significant heat transfer and soil water redistribution for sub-freezing temperature, for example,

91   in simplified SiB and BATS (Xue et al., 1991; Dickinson et al., 1993; Niu and Zeng, 2012). Koren

92   et al. (1999) suggested that the frozen soil is permeable due to macropores that exist in soil

93   structural aggregates, such as cracks, dead root passages, and worm holes. The NoahV3 model

94   adopted this scheme as its default option. Niu and Yang (2006) suggested to separate a model grid

95   into frozen and unfrozen patches, and these two patches have a linear effect on the soil hydraulic

96   properties. This treatment was incorporated into CLM 3.0 and Noah-MP in 2007 and 2011,

97   respectively.

98

99   The spatial heterogeneity of soil moisture and WTD requires high-resolution meteorological input

100   that direct outputs from GCMs are too coarse to provide. In GCMs, differences in simulated

101   precipitation stem from the choice of convection parameterization scheme (Sherwood et al., 2014;

102   Prein et al., 2015). An important approach to improve precipitation simulation is to conduct

103   dynamical downscaling using the convection-permitting model (CPM) (Ban et al., 2014; Prein et

104   al., 2015; Liu et al., 2017). The CPM uses a high spatial resolution (usually under 5-km) to

105   explicitly resolve convection without activating convection parameterization schemes. CPMs can

106   also improve the representation of fine-scale topography and spatial variations of surface fields

107   (Prein et al., 2013). These CPM added-values provide an excellent opportunity to investigate water

108   table dynamics in the PPR.

109

110   The objectives of this paper are to 1) investigate the performance of a regional scale coupled land-

111   groundwater model in simulating groundwater water levels, recharge and storage in a seasonally

112   frozen environment in PPR; and 2) explore the possible impacts of climate change on these

113   processes.

114

115   In this paper, we use a physical process-based LSM (Noah-MP) coupled with a groundwater

116   dynamics model (MMF model). The coupled Noah-MP-MMF model is driven by two sets of

117   meteorological forcing for 13 years under current and future climate scenarios. These two sets of

118   meteorological dataset are from a CPM dynamical downscaling project using the Weather

119   Research & Forecast (WRF) model with 4-km grid spacing covering the Contiguous U.S. and

120   Southern Canada (WRF CONUS, Liu et al., 2017). The paper is structured as follows: Section 2

121   introduces the groundwater observations for WTD evaluation in the PPR, the coupled Noah-MP-

122   MMF model, and the meteorological forcing from the WRF CONUS project. Section 3 evaluates

123   the model simulated WTD timeseries and shows the groundwater budget and hydrological changes

124   due to climate change. Section 4 and 5 offer a broad discussion and conclusion.

125   2. Data and Methods

126   2.1 Observational data

127   Groundwater observation data were obtained through several agencies: (1) the United States

128   Geological Survey (USGS) National Water Information System in the U.S.

129   (https://waterdata.usgs.gov/nwis/gw), (2) the Alberta Environment

130   (http://aep.alberta.ca/water/programs-and-services/groundwater/groundwater-observation-well-

131   network/default.aspx), (3) the Saskatchewan Water Security Agency

132   (https://www.wsask.ca/Water-Info/Ground-Water/Observation-Wells/).

133

134   Initially, groundwater data from 160 wells were acquired, 72 in the U.S., 43 from Alberta, and 45

135   from Saskatchewan. We used the following criteria to select qualified stations for our study and

136   evaluate our model performance against these observations:

137   1) the location of the wells are within the PPR region;

138   2) a sufficiently long data record exists during the simulation period. We define the

139   observation availability as the available observation period within the 13-year simulation

140   period and select wells with observation availability greater than 80%;

141   3) we only take data from unconfined aquifers with shallow groundwater levels (mean WTD >

142   5 m);

143   4) we only take data with minimal anthropogenic effects (such as from pumping or irrigation).

144
145   These criteria reduced the observation data to 33 well records, with six in Alberta, 13 in

146   Saskatchewan and 14 from the U.S. **Table 1** summarizes the information for each selected well,

147   and **Fig. 1**(a) shows the location of the wells in our study area. It is noteworthy that most of the

148   groundwater sites have more permeable deposits (sand and gravel) as provincial and state agencies

149   don't monitor low permeability formations. More information about the selecting criteria are

150   provided in the supplemental materials.

151

152   **Fig. 1** (a) Topography of the Prairie Pothole Region (PPR) and station location of rain gauges (black dots) and

153   groundwater wells (red diamonds); (b) Topography of the WRF CONUS domain, with the black box indicating the

154   PPR domain.

155

156   **Table 1.** Summary of the locations and aquifer type and soil type of the 33 selected wells.
157
158

159   2.2 Groundwater and Frozen Soil Scheme in Noah-MP

160   In the present study, we used the community Noah-MP LSM (Niu et al. 2011; Yang et al. 2011),

161   coupled with a GW model – the MMF model (Fan et al. 2007; Miguez-Macho et al., 2007). This

162   coupled model has been applied in many regional hydrology studies in offline mode (Miguez-

163   Macho and Fan 2012; Martinez et al., 2016) and coupled with regional climate models (Anyah et

164   al., 2008; Barlage et al., 2015). We present here a brief introduction to the MMF groundwater

165   scheme and the frozen soil scheme in Noah-MP, further details can be found in previous studies

166   (Fan et al., 2007;Miguez-Macho et al., 2007; Niu and Yang, 2006).

167

168   Fig. 2 is a diagram of the structure of 4 soil layers (0.1, 0.3, 0.6 and 1.0 m) and the underlying

169   unconfined aquifer in Noah-MP-MMF. The MMF scheme defines explicitly an unconfined aquifer

170   below the 2-m soil and an auxiliary soil layer stretching to the WTD, which varies in space and

171   time [m]. The thickness of this auxiliary layer (z_{aux} [m]) is also variable, depending on the WTD:

172   $$z_{aux} = \begin{cases} 1, & WTD \geq -3 \\ -2 - WTD, & WTD < -3 \end{cases} \quad (1)$$

173

174   The vertical fluxes include gravity drainage and capillary flux, solved from the Richards' equation,

175   $$q = K_\theta \left(\frac{\partial \psi}{\partial z} - 1 \right), \quad K_\theta = K_{sat} * \left(\frac{\theta}{\theta_{sat}} \right)^{2b+3}, \quad \psi = \psi_{sat} * \left(\frac{\theta_{sat}}{\theta} \right)^b \quad (2)$$

176   where q is water flux between two adjacent layers [m/s], K_θ is the hydraulic conductivity [m/s] at

177   certain soil moisture content θ [m^3/m^3], ψ is the soil matric potential [m] and b is soil pore size

178   index. The subscript *sat* denotes saturation. The recharge flux from/to the layer above WTD, R,

179   can be obtained according to WTD:

180
$$R = \begin{cases} K_k * \left(\dfrac{\psi_i - \psi_k}{z_{soil(i)} - z_{soil(k)}} - 1 \right), & WTD \geq -2 \\ K_{aux} * \left(\dfrac{\psi_4 - \psi_{aux}}{(-2) - (-3)} - 1 \right), & -2 > WTD \geq -3 \\ K_{sat} * \left(\dfrac{\psi_{aux} - \psi_{sat}}{(-2) - (WTD)} - 1 \right), & WTD < -3 \end{cases} \quad (3)$$

181

182   In the first case, WTD is in the resolved soil layers and z_{soil} is the depth of soil layer with the

183   subscript k indicating the layer containing WTD while i is the layer above. The calculated water

184   table recharge is then passed to the MMF groundwater routine.

185

186   The change of groundwater storage in the unconfined aquifer considers three components:

187   recharge flux (R), river discharge (Q_r), and lateral flows (Q_{lat}):

188   $$\Delta S_g = (R - Q_r + \sum Q_{lat}) \quad (4)$$

189   where S_g [mm] is groundwater storage, Q_r [mm] is the water flux of groundwater-river exchange,

190   and $\sum Q_{lat}$ [mm] are groundwater lateral flows to/from all surrounding grid cells. The groundwater

191   lateral flow ($\sum Q_{lat}$) is the total horizontal flows between each grid cell and its neighbouring grid

192   cells, calculated from Darcy's law with the Dupuit–Forchheimer approximation (Fan and Miguez-

193   Macho 2010), as:

194   $$Q_{lat} = wT \left(\dfrac{h - h_n}{l} \right) \quad (5)$$

195   where w is the width of cell interface [m], T is the transmissivity of groundwater flow [m²/s], h

196   and h_n are the water table head [m] of local and neighboring cell, and l is the length [m] between

197   cells. T depends on hydraulic conductivity K and WTD:

198
$$T = \begin{cases} \int_{-\infty}^{h} K\,dz & WTD \geq -2 \\ \int_{-\infty}^{(z_{surf}-2)} K\,dz + \sum K_i * dz_i & WTD < -2 \end{cases} \qquad (7)$$

199   For $WTD < -2$, K is assumed to decay exponentially with depth, $K = K_4 \exp(-z/f)$, K_4 is the

200   hydraulic conductivity in the 4-th soil layer and f is the e-folding length and depends on terrain

201   slope. For WTD ≥ -2, i represents the number of layers between the water table and the 2-m bottom

202   and z_{surf} is the surface elevation.

203

204   The river flux (Q_r) is also represented by a Darcy's law–type equation, where the flux depends on

205   the gradient between the groundwater and the river depth and the riverbed conductance:

206
$$Q_r = RC \cdot (h - z_{river}) \qquad (8)$$

207   with z_{river} is the depth of river [m] and RC is dimensionless river conductance, which depends on

208   the slope of the terrain and equilibrium water table. Eq. (8) is a simplification which uses z_{river}

209   rather than the water level in the river and, for this study, we only consider one-way discharge

210   from groundwater to rivers. Finally, the change of WTD is calculated as the total fluxes fill or

211   drain the pore space between saturation and the equilibrium soil moisture state (θ_{eq} [m³/m³]) in

212   the layer containing WTD:

213
$$\Delta\text{WTD} = \frac{\Delta S_g}{(\theta_{sat} - \theta_{eq})} \qquad (9)$$

214   If ΔS_g is greater than the pore space in the current layer, the soil moisture content of current layer

215   is saturated and the WTD rises to the layer above, updating the soil moisture content in the layer

216   above as well. Vice versa for negative ΔS_g as water table declines and soil moisture decreases.

217

218   **Fig. 2** Structure of the Noah-MP LSM coupled with MMF groundwater scheme, the top 2-m soil of 4 layers whose

219   thicknesses are 0.1, 0.3, 0.6 and 1.0 m. An unconfined aquifer is added below the 2-m boundary, including an auxiliary

220   layer and the saturated aquifer. Positive flux of R denotes downward transport. Two water table are shown, one within

221   the 2-m soil and one below, indicating that the model is capable to deal with both shallow and deep water table.

222

223   There are two options in Noah-MP LSM for frozen soil permeability; option 1, the default option

224   in Noah-MP, is from Niu and Yang (2006) and option 2 is inherited the Koren et al. (1999) scheme

225   from NoahV3. Option 1 assumes that a model grid cell consists of permeable and impermeable

226   patches and the area weighted sum of these patches gives the grid cell soil hydraulic properties.

227   Thus, the total soil moisture (θ) in the grid cell is used to compute hydraulic properties as:

228
$$\theta = \theta_{ice} + \theta_{liq} \qquad (10)$$

229
$$K = \left(1 - F_{frz}\right)K_u = \left(1 - F_{frz}\right)K_{sat}\left(\frac{\theta}{\theta_{sat}}\right)^{2b+3} \quad (11)$$

230   the subscript *frz* and *u* denote the frozen and unfrozen patches in the grid point. The impermeable

231   frozen soil fraction is parameterized as:

232
$$F_{frz} = e^{-\alpha(1-\theta_{ice}/\theta_{sat})} - e^{-\alpha} \qquad (12)$$

233     $\alpha = 3.0$ is an adjustable parameter. The amount of the liquid water in soil layer is either θ_{liq} or

234     $\theta_{liq,max}$, the maximum amount of liquid water, which is calculated by a more general form of the

235   freezing-point depression equation:

236
$$\theta_{liq,max} = \theta_{sat}\left\{\frac{10^3 L_f\left(T_{soil} - T_{frz}\right)}{gT_{soil}\psi_{sat}}\right\}^{-\frac{1}{b}} \quad (13)$$

237   where T_{soil} and T_{frz} are soil temperature and freezing point [K]; L_f is the latent heat of fusion [J

238   kg^{-1}]; g is gravitational acceleration [m s^{-2}].

239

240   On the other hand, the option 2 uses only the liquid water volume to calculate hydraulic properties

241   and assumes a non-linear effect of frozen soil on permeability. Also, the option 2 uses a variant of

242   freezing-point depression equation with an extra term, $(1 + 8\theta_{ice})^2$, to account for the increased

243   interface between soil particles and liquid water due to the increase of ice crystals. Generally,

244   option 1 assumes that soil ice has a smaller effect on infiltration and simulates more permeable

245   frozen soil than option 2 (Niu et al., 2011). For this reason, the option 1 allows the soil water to

246   move and redistribute more easily within the frozen soil and we decide to use option 1 in our study.

247   2.3 Forcing Data

248   The output from the WRF CONUS dataset (Liu et al. 2017) are used as meteorological forcing to

249   drive the Noah-MP-MMF model. The WRF CONUS project consists of two simulations. The first

250   simulation is referred as the current climate scenario, or control run (CTRL), from Oct 2000 to Sep

251   2013, and forced with the 6-hourly 0.7° ERA-Interim reanalysis data. The second simulation is a

252   perturbation to reflect the future climate scenario, closely following the pseudo global warming

253   (PGW) approach in previous works (Rasmussen et al., 2014). The PGW simulation is forced with

254   6-hourly ERA-Interim reanalysis data plus a delta climate change signal derived from an ensemble

255   of CMIP5 models under the RCP8.5 emission scenario and reflects the climate change signal

256   between the end of 21st and 20th century.

257

258   **Fig. 3** shows the annual precipitation in the PPR from 4-km WRF CONUS from the current climate

259   and 32-km North America Regional Reanalysis (NARR, another reanalysis dataset commonly

260   used for land surface model forcing). Both datasets show similar annual precipitation pattern and

261   bias patterns compared to observations: underestimating of precipitation in the east and

262   overestimating in the west. However, the WRF CONUS shows significant improvement of

263   percentage bias in precipitation ((Model-Observation)/Observation) over the western PPR. For the

264   consistency of the same source of data for current and future climate, the WRF-CONUS is the best

265   available dataset for the coupled land-groundwater study in the PPR.

266

267   **Fig. 3** Evaluation of the annual precipitation from WRF CONUS (top) and NARR (bottom) against rain gauge

268   observation.

269

270   For the future climate study, the precipitation and temperature of the PGW climate forcing are

271   shown in **Fig. 4** and **Fig. 5**. The WRF CONUS projects more precipitation in the PPR, except in

272   the southeast of the domain in summer, where it shows a precipitation reduction of about 50 to 100

273   mm. On the other hand, the WRF CONUS projects strongest warming occurring in the northeast

274   PPR in winter (**Fig. 5**), about 6–8 °C. Another significant warming signal occurs in summer in the

275   southeast of domain, corresponding to the reduction of future precipitation, as seen in **Fig. 4**.

276

277   **Fig. 4** Seasonal accumulated precipitation from current climate scenario(CTRL), future climate scenario (PGW) and

278   projected change (PGW-CTRL) in the forcing data.

279

280   **Fig. 5** Seasonal averaged temperature from CTRL, PGW, and the projected change (PGW-CTRL).

281

282 2.4 Model Setup

283 The two Noah-MP-MMF simulations representing the current climate and future climate are

284 denoted as CTRL and PGW, respectively. The initial groundwater levels are from a global 1-km

285 equilibrium groundwater map (Fan et al., 2013) and the equilibrium soil moisture for each soil

286 layer is calculated at the first model timestep with climatology recharge, spinning up for 500 years.

287 Since the model domain is at a different resolution than the input data, the appropriate initial WTD

288 at 4-km may be different than the average at 1-km. To properly initialize the simulation, we spin

289 up the model using the forcing of current climate (CTRL) for the years from 2000 to 2001

290 repeatedly (in total 10 loops).

291

292 Due to different data sources, the default soil types along the boundary between the U.S. and

293 Canada are discontinuous. Thus, we use the global 1-km fine soil data (Shangguan et al., 2014,

294 http://globalchange.bnu.edu.cn/research/soilw) in our study region. The soil properties for the

295 aquifer use the same properties as the lowest soil layer from the Noah-MP 2-m soil layers.

296   3. Results

297   3.1 Comparison with groundwater observations

298   According to the locations of 33 groundwater wells in **Table 1**, the simulated WTD from the

299   closest model grid points are extracted. **Fig. 6** shows the modeled WTD bias from the CTRL run.

300   We also select the monthly WTD timeseries from 8 sites, the observation are in black dots and

301   CTRL in blue lines. See supplemental materials for the timeseries of 33 sites. The model produces

302   reasonable values of mean WTD, the mean bias are smaller than 1 m in most of sites, except in

303   Alberta, where the model predicts deep bias about 5 m in the northwestern part of PPR. The model

304   also successfully captures the annual cycle of WTD, which rises in spring and early summer,

305   because of snowmelt and rainfall recharge, and declines in summer and fall, because of high ET,

306   and in winter because of frozen near-surface soil. In all observations, the timing of the water table

307   rising and dropping is well simulated, as the timing and amount of infiltration and recharge in

308   spring is controlled by the freeze-thaw processes in seasonally frozen soil.

309

310   **Fig. 6.** WTD (m) bias from CTRL simulation and timeseries from 8 groundwater wells in PPR (black for observation and
311   blue for CTRL model simulation). See Table 2 CTRL column for the model statistics and supplemental materials for complete
312   timeseries from 33 wells.
313

314   On the other hand, the model simulated WTD seasonal variation is smaller than observations. The

315   small seasonal variation could be due to the misrepresentation between the lithology from the

316   observational surveys and the soil types in the model grids. As mentioned in Section 2.2, the

317   groundwater aquifer uses the same soil types as the bottom layer of the resolved 2-m soil layers.

318   While sand and gravel are the dominant lithology in most of the sites, they are mostly clay and

319   loam in the model (Table 1). For sandy soil reported in most of the sites, small capacity and fast

320   responses to infiltration lead to large water table fluctuations, whereas, in the model, clay and loam

321 soil allows low permeability and large capacity, and smoothens responses to recharge and capillary

322 effects. Furthermore, the 4-layer soils are vertically homogeneous in soil type and the groundwater

323 model uses the lowest level soil type as the aquifer lithology. For many part of the PPR, where

324 groundwater level are perched at the top 5-m due to a layer called glacial till. These

325 geohydrological characteristics cannot be reflected in this model and contribute to the deep WTD

326 bias simulated in Alberta. This shortcoming of the model was also reported in a study taken place

327 in the Amazon rainforest (Miguez-Macho et al., 2012).

328

329 3.2 Climate change signal in Groundwater fluxes

330 The MMF groundwater model simulates three components in the groundwater water budget, the

331 recharge flux (R), lateral flow (Q_{lat}), and discharge flux to rivers (Q_r). Because the topography is

332 usually flat in the PPR, the magnitude of groundwater lateral transport is very small (Q_{lat} less than

333 5 mm per year). On the other hand, the shallow water table in the PPR region is higher than the

334 local river bed, thus, the Q_r term is always discharging from groundwater aquifers to rivers. As a

335 result, the recharge term is the major contributor to the groundwater storage in the PPR, and its

336 variation (usually between -100 to 100 mm) dominates the timing and amplitude of the water table

337 dynamics. The seasonal accumulated total groundwater fluxes in the PPR ($R+Q_{lat} - Q_r$) are

338 shown in **Fig. 7**. The positive (negative) flux in blue (red) means the groundwater aquifer is gaining

339 (losing) water, causing the water table to rise (decline).

340

341 **Fig. 7** Seasonal accumulated total groundwater fluxes ($R+$) for current climate (CTRL, top), future climate (PGW,
342 middle) and projected change (PGW-CTRL, bottom) in forcing data. Black dashed lines in PGW-CTRL separate the
343 PPR into eastern and western halves.
344

345 Under current climate conditions, the total groundwater fluxes show strong seasonal fluctuations,

346 consistent with the WTD timeseries shown in **Fig. 6**. On average, in fall (SON) and winter (DJF),

347 there is a 20-mm negative recharge, driven by the capillary effects and drawing water from aquifer

348 to dry soil above. Spring (MAM) is usually the season with a strong positive recharge because

349 snowmelt provides a significant amount of water, and soils thawing allow infiltration. The large

350 amount of snowmelt water contributes to more than 100 mm of positive recharge in the eastern

351 domain. It is until summer (JJA), when strong ET depletes soil moisture and results in about 50

352 mm of negative recharge.

353

354   Under future climate conditions, the increased PR in fall and winter leads to wetter upper soil

355   layers, resulting in a net positive recharge flux (PGW – CTRL in SON and DJF). However, the

356   PGW summer is impacted by increased ET under a warmer and drier climate, due to higher

357   temperature and less PR. As a result, the groundwater uptake by the capillary effect is more critical

358   in the future summer. Furthermore, there is a strong east-to-west difference in the total

359   groundwater flux change from PGW to CTRL. In the eastern PPR, the change in total groundwater

360   flux exhibits obvious seasonality while the model projects persistent positive groundwater fluxes

361   in the western PPR.

362

363   3.3 Water budget analysis

364   **Fig. 8** and **Fig. 9** show the water budget analysis for the eastern and western PPR (divided by the

365   dotted line in 103° W in Fig. 7), respectively. Four components are presented in the figures, i.e.

366   (1) PR and ET; (2) surface and underground runoff (*SFCRUN* and *UDGRUN*); and surface

367   snowpack; (3) the change of soil moisture storage and (4) groundwater fluxes and the change of

368   storage. In the current and future climate, these budget terms are plotted in annual accumulation

369   ((a) and (b) for CTRL and PGW), whereas their difference are plotted in each month individually

370   ((c) for PGW-CTRL).

371

372   Under current climate conditions, during snowmelt infiltration and rainfall events, water infiltrates

373   into the top soil layer, travels through the soil column and exits the bottom of the 2-m boundary,

374   hence, the water table rises. During the summer dry season, ET is higher than PR and the soil

375   layers lose water through ET, therefore, the capillary effect takes water from the underlying aquifer

376   and the water table declines. In winter, the near-surface soil in the PPR is seasonally frozen, thus,

377   a redistribution of subsurface water to the freezing front results in negative recharge, and the water

378   table declines.

379

380   In the eastern PPR, the effective precipitation (PR-ET) is found to increase from fall to spring, but

381   decrease in summer in PGW (**Fig. 8**(1c)). Warmer falls and winters in PGW, together with

382   increased PR, not only delay snow accumulation and bring forward snowmelt, but also change

383   the precipitation partition – more as rain and less as snow. This warming causes up to 20 mm of

384   snowpack loss (**Fig.8**(2c)). The underground runoff starts much earlier in PGW (December)

385   (**Fig.8**(2b)) than in CTRL (February) (**Fig.8**(2a)). On the other hand, the warming in PGW also

386   changes the partitioning of soil ice and soil water in subsurface soil layers (**Fig**. 8(3c)). For late

387   spring in PGW, the springtime recharge in the future is significantly reduced due to early melting

388   and less snowpack remaining (**Fig. 8**(4c)). In the PGW summer, reduced PR (50 mm less) and

389   higher temperatures (8 °C warmer) lead to reduction in total soil moisture, and a stronger negative

390   recharge from the aquifer. Therefore, the increase of recharge from fall to early spring compensates

391   the recharge reduction due to stronger ET in summer in the eastern PPR, and changes little in the

392   annual mean groundwater storage (1.763 mm per year).

393

394   **Fig. 8** Water budget analysis in the eastern PPR in (a) CTRL, (b) PGW and (c) PGW – CTRL. Water budget terms

395   include: (1) *PR & ET*, (2) surface snow, surface runoff and underground runoff (*SNOW*, *SFCRUN*, and *UDGRUN*),

396   (3) change of soil moisture storage (soil water, soil ice and total soil moisture, ΔSMC) and (4) groundwater fluxes

397   and the change of groundwater storage (R, Q_{lat}, Q_r, ΔS_g). The annual mean soil moisture change (PGW-CTRL) is

398   shown with black dashed line in (3). The Residual term is defined as $Res = (R+Q_{lat}-Q_r)-\Delta S_g$ in (4). Note that in (a)

399   and (b) the accumulated fluxes and change in storage are shown in lines, whereas in (c) the difference in (PGW-CTRL)

400   is shown for each individual month in bars.

401

402   These changes in water budget components in the western PPR (**Fig. 9**) are similar to those in the

403   eastern PPR (**Fig. 8**), except in summer. The reduction in summer PR in the western the PPR (less

404   than 5 mm reduction) is not as obvious as that in the eastern PPR (50 mm reduction) (**Fig. 4**). Thus,

405   annual mean total soil moisture in future is about the same as in current climate (Fig. 9(3c)) and

406   results in little negative recharge in PGW summer (**Fig. 9**(4c)). Therefore, the increase in annual

407   recharge is more significant (10 mm per year), an increase of about 50% of the annual recharge in

408   the current climate (20 mm per year) (**Fig. 9**(4c)).

409

410 **Fig. 9** Same as Fig. 8. Water budget analysis in the **western PPR**: in (a) CTRL, (b) PGW and (c) PGW – CTRL.
411 Water budget terms include: (1) *PR & ET*, (2) surface snow, surface runoff and underground runoff (*SNOW*, *SFCRUN*,
412 and *UDGRUN*), (3) change of soil moisture storage (soil water, soil ice and total soil moisture, ΔSMC) and (4)
413 groundwater fluxes and the change of groundwater storage (R, Q_{lat}, Q_r, ΔS_g). The annual mean soil moisture change
414 (PGW-CTRL) is shown with black dashed line in (3). The Residual term is defined as $Res = (R+Q_{lat}-Q_r)-\Delta S_g$ in (4).
415 Note that in (a) and (b) the accumulated fluxes and change in storage are shown in lines, whereas in (c) the difference
416 in (PGW-CTRL) is shown for each individual month in bars.
417

418 In both the eastern and western PPR, the water budget components for the groundwater aquifer are

419 plotted in **Fig. 8**(4) and **Fig. 9** (4), with the changes of each flux (PGW-CTRL) printed at the

420 bottom. The groundwater lateral flow is a small term in areal average and has little impact on the

421 groundwater storage. Nearly half of the increased recharge in both the eastern and western PPR is

422 discharged to river flux (Q_r = 2.26 mm out of R = 4.15 mm in the eastern PPR and Q_r = 5.20 mm

423 out of R = 10.72 mm in western PPR). Therefore, the groundwater storage change in the eastern

424 PPR (1.76 mm per year) is not as great as that in the western PPR (5.39 mm per year).

425

426 These two regions of the PPR show differences in hydrological response to future climate because

427 of the spatial variation of the summer PR. As shown in both **Fig. 4** (PGW-CTRL), **Fig. 8**(1) and

428 **Fig. 9**(1), the reduction of future PR in summer in the eastern PPR is significant (50 mm). The

429 spatial difference of precipitation changes in the PPR further results in the recharge increase

430 doubling in the western PPR compared to the eastern PPR.

431

432 4. Discussion

433 4.1 Improving WTD Simulation

434 In Section 3.1, we show that the model is capable of simulating the mean WTD in most sites, yet

435 predicts deep groundwater in Alberta and underestimates its seasonal variation. These results may

436 be due to misrepresentations between model default soil type and the soil properties in the

437 observational wells. To test this theory, an additional simulation, REP, is conducted by replacing

438 the default soil types in the locations of these 33 groundwater wells with sand-type soil, which is

439 the dominant soil types reported from observational surveys. The timeseries of the REP and default

440 CTRL are shown in Fig. 10 (also see supplemental materials for the complete 33 sites) and a

441 summary of the mean and standard deviation of the two simulations are provided in Table 2.

442

443 **Fig. 10** Same as Fig. 6, WTD (m) bias from CTRL simulation and timeseries from 8 groundwater wells in PPR (black for
444 observation and blue for CTRL model simulation, and red for the replacing soil type simulation). REP is the additional
445 simulation by replacing the default soil type in the model with sandy soil type.
446

447 The REP simulation with sandy soil show two sensitive signals: (1) REP WTD are shallower than

448 the default simulation; (2) and exhibit stronger seasonal variation. These two signals can be

449 explained by the WTD equation in the MMF scheme:

450 $$\Delta WTD = \frac{\Delta(R + Q_{lat} - Q_r)}{(\theta_{sat} - \theta_{eq})} \quad (14)$$

451 Eq. (14) represents that the change of WTD in a period of time is calculated by the total

452 groundwater fluxes, $\Delta(R + Q_{lat} - Q_r)$, divided by the available soil moisture capacity of current

453 layer ($\theta_{sat} - \theta_{eq}$). In REP simulation, the parameters θ_{sat} for the dominant soil type in

454 observational sites (sand/gravel) is smaller than those in default model grids (clay loam, sandy

455 loam, loam, loamy sand, etc.). Therefore, changing the θ_{sat} is essentially reducing the storage in

456 the aquifer and soil in this model grid. Given the same amount of groundwater flux, in the REP

457 simulation, the mean WTD is higher and the seasonal variation is stronger than the default CTRL

458 run.

459

460 In the REP simulation, we replaced soil type only at a limited number of sites because the

461 geological survey data in high resolution and large area extent is not yet available for the whole

462 PPR. At point scale, the WTD responses to climate change over these limited number of sites show

463 diverse results and uncertainties (see supplemental materials). For the rest of the domain, the

464 default soil type from global 1-km soil map is used. The REP modifications of soil types at point-

465 scale have small contribution to the water balance analysis (Fig. 8 & 9) at regional-scale. Our

466 results and conclusions for groundwater response to PGW doesn't change. We are currently

467 undertaking a soil property survey project in the PPR region to obtain soil properties at high spatial

468 resolution, both horizontal and vertical. This may provide better opportunity to improve WTD

469 simulation as well as assess climate-groundwater interaction in future studies.

470

471 4.2 Climate Change Impacts on Groundwater Hydrological Regime

472 The warming and increased precipitation in cold seasons in future climate lead to later snow

473 accumulation, higher recharge in winter and earlier melting in spring compared to current climate.

474 Such changes in snowpack loss have been hypothesized in mountainous as well as high-latitude

475 regions (Taylor et al 2013; Ireson et al., 2015; Meixner et al., 2016; Musselman et al., 2017). In

476 addition to the amount of recharge, the shift of recharge season is also noteworthy. Under current

477 climate conditions in spring, soil thawing (in March) is generally later than snowmelt (in February)

478 by a month in the PPR. Thus, the snowmelt water in pre-thaw spring would either re-freeze after

479   infiltrating into partially frozen soil or become surface runoff. Under the PGW climate, the warmer

480   winter and spring allows snowmelt and soil thaw to occur earlier in the middle of winter (in January

481   and February, respectively). As a result, the recharge season starts earlier in December, and last

482   longer until June, results in longer recharge season but with lower recharge rate.

483

484   Future projected increasing evapotranspiration demand in summer desiccates soil moisture,

485   resulting in more water uptake from aquifers to subsidize dry soil in the future summer. This

486   groundwater transport to soil moisture is similar to the "buffer effect" documented in an offline

487   study in the Amazon rainforest (Pokhrel et al., 2014). In , shallow water tables exist in the critical

488   zone, where WTD ranges from 1 to 5 meters below surface and could exert strong influence on

489   land energy and moisture fluxes feedback to the atmosphere (Kollet and Maxwell, 2008; Fan ,

490   2015). Previous coupled atmosphere-land-groundwater studies at 30-km resolution showed that

491   groundwater could support soil moisture during summer dry period, but has little impacts on

492   precipitation in Central U.S. (Barlage et al., 2015). It would be an interesting topic to study the

493   integrated impacts of shallow groundwater to regional climate in the convection permitting

494   resolution (resolution < 5-km).

495

496   4.3 Fine-scale interaction between groundwater and Prairie pothole wetlands

497   Furthermore, groundwater exchange with prairie pothole wetlands are complicated and critical in

498   the PPR. Numerous wetlands known as potholes or sloughs provide important ecosystem services,

499   such as providing wildlife habitats and groundwater recharge (Johnson et al., 2010). Shallow

500   groundwater aquifers may receive water from or lose water to prairie wetlands depending on the

501   hydrological setting. Depression-focused recharge generated by runoff from upland to depression

502   contributes to sufficient amount of water input to shallow groundwater (5-40 mm/year) (Hayashi

503   et al., 2016).

504

505   On the other hand, groundwater lateral flow exchange center of a wetland pond to its moist margin

506   is also an important component in the wetland water balance (van der Kamp and Hayashi, 2009;

507   Brannen, et al., 2015; Hayashi et al., 2016). However, this groundwater-wetland exchange

508   typically occurs on local scale (from 10 to 100 m) and thus, is challenging to represent in current

509   land surface models or climate models (resolution from 1 km to 100 km). In this paper, we focus

510   on the groundwater dynamics on regional scale, which is still unable to capture these small wetland

511   features in this study. We admit this limitation and are currently developing a sub-grid scheme to

512   represent small scale open water wetlands as a fraction within a grid cell and calculate its feedback

513   to regional environments. Future studies on this topic will provide valuable insights on these key

514   ecosystems and their interaction under climate change.

515

516   Conclusion

517   In this study, a coupled land-groundwater model is applied to simulate the interaction between the

518   groundwater aquifer and soil moisture in the PPR. The climate forcing is from a dynamical

519   downscaling project (WRF CONUS), which uses the convection-permitting model (CPM)

520   configuration in high resolution. The goal of this study is to investigate the groundwater responses

521   to climate change, and to identify the major processes that contribute to these responses in the PPR.

522   To our knowledge, this is the first study applying CPM forcing in a hydrology study in this region.

523   We have three main findings:

524

525   (1) the coupled land-groundwater model shows reliable simulation of mean WTD, however

526   underestimates the seasonal variation of the water table against well observations. This could be

527   attributed to several reasons, including misrepresentation of topography and soil types, as well as

528   vertical homogenous soil layers used in the model. We further conducted an additional simulation

529   (REP) by replacing the model default soil types with sand-type soil and the simulated WTDs were

530   improved in both mean and seasonal variation. However, inadequacy of soil properties in deeper

531   layer and higher spatial resolution is still a limitation.

532

533   (2) Recharge markedly increases due to projected increased PR, particularly from fall to spring

534   under future climate conditions. Strong east-west spatial variation exists in the annual recharge

535   increases, 25% in the eastern and 50% in the western PPR. This is due to the significant projected

536   PR reduction in PGW summer in the eastern PPR but little change in the western PPR. This PR

537   reduction leads to stronger ET demand, which draws more groundwater uptake due to the capillary

538   effect, results in negative recharge in the summer. Therefore, the increased recharge from fall to

539   spring is consumed by ET in summer, and results in little change in groundwater in the eastern

540   PPR, while gaining water in the western PPR.

541

542   (3) The timing of infiltration and recharge are critically impacted by the changes in freeze-thaw

543   processes. Increased precipitation, combined with higher winter temperatures, results in later snow

544   accumulation/soil freezing, partitioned more as rain than snow, and earlier snowmelt/soil thaw.

545   This leads to substantial loss of snowpack, shorter frozen soil season, and higher permeability in

546   soil allowing infiltration. Late accumulation/freezing and early melting/thawing leads to an early

547   start of a longer recharge season from December to June, but with a lower recharge rate.

548

549   Our study has some limitations where future studies are encouraged:

550   (1) Despite the large number of groundwater wells in PPR, only a few are suitable for long-term

551   evaluation, due to data quality, anthropogenic pumping, and length of data record. As remote

552   sensing techniques advance, observing terrestrial water storage anomalies derived from the

553   GRACE satellite may provide substantial information on WTD, although the GRACE information

554   needs to be downscaled to a finer scale before comparisons can be made with regional hydrology

555   models at km-scale (Pokhrel et al., 2013).

556

557   (2) This study is an offline study of climate change impacts on groundwater. It is important to

558   investigate how shallow groundwater in the earth's critical zone could interact with surface water

559   and energy exchange to the atmosphere and affect regional climate. This investigation would be

560   important to the central North America region (one of the land atmosphere coupling "hot spots",

561   Koster et al., 2004).

562

Acknowledgments

The authors Zhe Zhang, Yanping Li, Zhenhua Li gratefully acknowledge the support from the Changing Cold Regions Network (CCRN) funded by the Natural Science and Engineering Research Council of Canada (NSERC), as well as the Global Water Future project and Global Institute of Water Security at University of Saskatchewan. Yanping Li acknowledge the support from NSERC Discovery Grant. Fei Chen, Michael Barlage appreciate the support from the Water System Program at the National Center for Atmospheric Research (NCAR), USDA NIFA Grants 2015-67003-23508 and 2015-67003-23460, NSF INFEW/T2 Grant #1739705, and NOAA CFDA Grant #NA18OAR4590381. NCAR is sponsored by the National Science Foundation. Any opinions, findings, conclusions or recommendations expressed in this publication are those of the authors and do not necessarily reflect the views of the National Science Foundation.

575   Reference

576 Anyah, R. O., Weaver, C. P., Miguez-macho, G., Fan, Y. and Robock, A.: Incorporating water
577   table dynamics in climate modeling : 3 . Simulated groundwater influence on coupled land-
578   atmosphere variability, , 113, 1–15, doi:10.1029/2007JD009087, 2008.

579 Ban, N., Schmidli, J. and Schär, C.: Evaluation of the new convective-resolving regional climate
580   modeling approach in decade-long simulations, J. Geophys. Res. Atmos., 119, 7889–7907,
581   doi:10.1002/2014JD021478.Received, 2014.

582 Barlage, M., Tewari, M., Chen, F., Miguez-Macho, G., Yang, Z. L. and Niu, G. Y.: The effect of
583   groundwater interaction in North American regional climate simulations with WRF/Noah-MP,
584   Clim. Change, 129(3–4), 485–498, doi:10.1007/s10584-014-1308-8, 2015.

585 Brannen, R., Spence, C. and Ireson, A.: Influence of shallow groundwater-surface water
586   interactions on the hydrological connectivity and water budget of a wetland complex, Hydrol.
587   Process., 29(18), 3862–3877, doi:10.1002/hyp.10563, 2015.

588 Christensen NS, Wood AW, Voisin N, et al (2004) The Effects of Climate Change on the
589   Hydrology and Water Resources of the Colorado River Basin. Clim Change 62:337–363. doi:
590   10.1023/B:CLIM.0000013684.13621.1f

591 Dickinson RE, Henderson-Sellers A, Kennedy PJ (1993) Biosphere-Atmosphere Transfer Scheme
592   (BATS) Version le as Coupled to the NCAR Community Climate Model. NCAR Technical
593   Note, NCAR/TN-387+STR.

594 Döll, P. and Fiedler, K.: Global-scale modeling of groundwater recharge, Hydrol. Earth Syst. Sci.,
595   12(3), 863–885, doi:10.5194/hess-12-863-2008, 2008.

596 Döll, P.: Vulnerability to the impact of climate change on renewable groundwater resources: A
597   global-scale assessment, Environ. Res. Lett., 4(3), doi:10.1088/1748-9326/4/3/035006, 2009.

598 Dumanski, S., Pomeroy, J. W. and Westbrook, C. J.: Hydrological regime changes in a Canadian
599   Prairie basin, Hydrol. Process., 29(18), 3893–3904, doi:10.1002/hyp.10567, 2015.

600 Environment Canada: Municipal Water Use, 2009 Statistics, 2011 Munic. Water Use Rep., 24,
601   doi:En11-2/2009E-PDF Information, 2011.

602 Fan Y, Miguez-Macho G, Weaver CP, et al (2007) Incorporating water table dynamics in climate
603   modeling: 1. Water table observations and equilibrium water table simulations. J Geophys
604   Res Atmos 112:1–17. doi: 10.1029/2006JD008111

605 Fan, Y., Li, H. and Miguez-Macho, G.: Global patterns of groundwater table depth, Science (80-.).,
606   339(6122), 940–943, doi:10.1126/science.1229881, 2013.

607 Fan, Y.: Groundwater in the Earth's critical zones: Relevance to large-scale patterns and processes,
608   Water Resour. Res., 3052–3069, doi:10.1002/2015WR017037.Received, 2015.

609 Granger RJ, Gray DM: Evaporation from natural non-saturated surface. J. Hydrol., 111, 21–29,
610   1989.

611 Gray DM: Handbook on the Principles of Hydrology: With Special Emphasis Directed to Canadian
612   Conditions in the Discussion, Applications, and Presentation of Data. Water Information
613   Center: Huntingdon, New York, 1970. ISBN:0-912394-07-2

614 Green, T. R., Taniguchi, M., Kooi, H., Gurdak, J. J., Allen, D. M., Hiscock, K. M., Treidel, H. and
615   Aureli, A.: Beneath the surface of global change: Impacts of climate change on groundwater,
616   J. Hydrol., 405(3–4), 532–560, doi:10.1016/j.jhydrol.2011.05.002, 2011.

617 Hayashi, M., Van Der Kamp, G. and Schmidt, R.: Focused infiltration of snowmelt water in
618   partially frozen soil under small depressions, J. Hydrol., 270(3–4), 214–229,
619   doi:10.1016/S0022-1694(02)00287-1, 2003.

Hayashi, M., van der Kamp, G. and Rosenberry, D. O.: Hydrology of Prairie Wetlands: Understanding the Integrated Surface-Water and Groundwater Processes, Wetlands, 36, 237–254, doi:10.1007/s13157-016-0797-9, 2016.

Ireson, A. M., van der Kamp, G., Ferguson, G., Nachshon, U. and Wheater, H. S.: Hydrogeological processes in seasonally frozen northern latitudes: understanding, gaps and challenges, Hydrogeol. J., 21(1), 53–66, doi:10.1007/s10040-012-0916-5, 2013.

Ireson, A. M., Barr, A. G., Johnstone, J. F., Mamet, S. D., van der Kamp, G., Whitfield, C. J., Michel, N. L., North, R. L., Westbrook, C. J., DeBeer, C., Chun, K. P., Nazemi, A. and Sagin, J.: The changing water cycle: the Boreal Plains ecozone of Western Canada, Wiley Interdiscip. Rev. Water, 2(5), 505–521, doi:10.1002/wat2.1098, 2015.

Johnson, W. C., Werner, B., Guntenspergen, G. R., Voldseth, R. A., Millett, B., Naugle, D. E., Tulbure, M., Carroll, R. W. H., Tracy, J. and Olawsky, C.: Prairie Wetland Complexes as Landscape Functional Units in a Changing Climate, Bioscience, 60(2), 128–140, doi:10.1525/bio.2010.60.2.7, 2010.

Kelln C, Barbour L, Qualizza C (2007) Preferential Flow in a Reclamation Cover : Hydrological and Geochemical Response. 1277–1289

Koren, V., Schaake, J., Mitchell, K., Duan, Q.-Y., Chen, F., & Baker, J. M. (1999). A parameterization of snowpack and frozen ground intended for NCEP weather and climate models. Journal of Geophysical Research: Atmospheres, 104(D16), 19569–19585. https://doi.org/10.1029/1999JD900232

Koster, R. D., Dirmeyer, P. A., Guo, Z., Bonan, G., Chan, E., Cox, P., Gordon, C. T., Kanae, S., Kowalczyk, E., Lawrence, D., Liu, P., Lu, C.-H., Malyshev, S., McAvaney, B., Mitchell, K., Mocko, D., Oki, T., Oleson, K., Pitman, A., Sud, Y. C., Taylor, C. M., Verseghy, D., Vasic, R., Xue, Y. and Yamada, T.: Regions of Strong Coupling Between Soil Moisture and Precipitation, Science (80-.)., 305(5687), 1138 LP-1140 [online] Available from: http://science.sciencemag.org/content/305/5687/1138.abstract, 2004.

Kollet SJ, Maxwell RM (2008) Capturing the influence of groundwater dynamics on land surface processes using an integrated, distributed watershed model. Water Resour Res 44:1–18. doi: 10.1029/2007WR006004

Kurylyk, B. L. and MacQuarrie, K. T. B.: The uncertainty associated with estimating future groundwater recharge: A summary of recent research and an example from a small unconfined aquifer in a northern humid-continental climate, J. Hydrol., 492, 244–253, doi:10.1016/j.jhydrol.2013.03.043, 2013.

Liu, C., Ikeda, K., Rasmussen, R., Barlage, M., Newman, A. J., Prein, A. F., Chen, F., Chen, L., Clark, M., Dai, A., Dudhia, J., Eidhammer, T., Gochis, D., Gutmann, E., Kurkute, S., Li, Y., Thompson, G. and Yates, D.: Continental-scale convection-permitting modeling of the current and future climate of North America, Clim. Dyn., 49(1–2), 71–95, doi:10.1007/s00382-016-3327-9, 2017.

Martinez, J. A., Dominguez, F. and Miguez-Macho, G.: Effects of a Groundwater Scheme on the Simulation of Soil Moisture and Evapotranspiration over Southern South America, J. Hydrometeorol., 17(11), 2941–2957, doi:10.1175/JHM-D-16-0051.1, 2016.

Maxwell RM, Miller NL (2005) Development of a Coupled Land Surface and Groundwater Model. 233–247

Maxwell, R. M. and Kollet, S. J.: Interdependence of groundwater dynamics and land-energy feedbacks under climate change, Nat. Geosci., 1(10), 665–669, doi:10.1038/ngeo315, 2008.

Maxwell, R. M., Condon, L. E. and Kollet, S. J.: A high-resolution simulation of groundwater and surface water over most of the continental US with the integrated hydrologic model ParFlow v3, Geosci. Model Dev., 8(3), 923–937, doi:10.5194/gmd-8-923-2015, 2015.

Meixner, T., Manning, A. H., Stonestrom, D. A., Allen, D. M., Ajami, H., Blasch, K. W., Brookfield, A. E., Castro, C. L., Clark, J. F., Gochis, D. J., Flint, A. L., Neff, K. L., Niraula, R., Rodell, M., Scanlon, B. R., Singha, K. and Walvoord, M. A.: Implications of projected climate change for groundwater recharge in the western United States, J. Hydrol., 534, 124–138, doi:10.1016/j.jhydrol.2015.12.027, 2016.

Miguez-Macho, G., Fan, Y., Weaver, C. P., Walko, R. and Robock, A.: Incorporating water table dynamics in climate modeling: 2. Formulation, validation, and soil moisture simulation, J.

Miguez-Macho, G. and Fan, Y.: The role of groundwater in the Amazon water cycle: 1. Influence on seasonal streamflow, flooding and wetlands, J. Geophys. Res. Atmos., 117(15), 1–30, doi:10.1029/2012JD017539, 2012.

Moeck, C., Brunner, P. and Hunkeler, D.: The influence of model structure on groundwater recharge rates in climate-change impact studies, Hydrogeol. J., 24(5), 1171–1184, doi:10.1007/s10040-016-1367-1, 2016.

Mohammed, A. A., Kurylyk, B. L., Cey, E. E. and Hayashi, M.: Snowmelt Infiltration and Macropore Flow in Frozen Soils: Overview, Knowledge Gaps, and a Conceptual Framework, Vadose Zo. J., 17(1), doi:10.2136/vzj2018.04.0084, 2018.

Musselman, K. N., Clark, M. P., Liu, C., Ikeda, K. and Rasmussen, R.: Slower snowmelt in a warmer world, Nat. Clim. Chang., 7(February), 214–220, doi:10.1038/NCLIMATE3225, 2017.

National Research Council: Groundwater fluxes across inter- faces. The National Academy Press, 85 pp, 2003

Niraula R, Meixner T, Dominguez F, et al (2017) How Might Recharge Change Under Projected Climate Change in the Western U.S.? Geophys Res Lett 44:10,407-10,418. doi: 10.1002/2017GL075421

Niu, G.-Y., & Yang, Z.-L. (2006). Effects of Frozen Soil on Snowmelt Runoff and Soil Water Storage at a Continental Scale. Journal of Hydrometeorology, 7(5), 937–952. https://doi.org/10.1175/JHM538.1

Niu G, Yang Z, Dickinson RE, Gulden LE (2007) Development of a simple groundwater model for use in climate models and evaluation with Gravity Recovery and Climate Experiment data. 112:1–14. doi: 10.1029/2006JD007522

Niu, G. Y., Yang, Z. L., Mitchell, K. E., Chen, F., Ek, M. B., Barlage, M., Kumar, A., Manning, K., Niyogi, D., Rosero, E., Tewari, M. and Xia, Y.: The community Noah land surface model with multiparameterization options (Noah-MP): 1. Model description and evaluation with local-scale measurements, J. Geophys. Res. Atmos., 116(12), 1–19, doi:10.1029/2010JD015139, 2011.

Niu G-Y, Zeng X (2012) Earth System Model, Modeling the Land Component of. In: Climate Change Modeling Methodology. Springer New York, New York, NY, pp 139–168

Pokhrel, Y. N., Fan, Y., Miguez-Macho, G., Yeh, P. J. F. and Han, S. C.: The role of groundwater in the Amazon water cycle: 3. Influence on terrestrial water storage computations and comparison with GRACE, J. Geophys. Res. Atmos., 118(8), 3233–3244, doi:10.1002/jgrd.50335, 2013.

Pokhrel, Y. N., Fan, Y. and Miguez-Macho, G.: Potential hydrologic changes in the Amazon by the end of the 21st century and the groundwater buffer, Environ. Res. Lett., 9(8), doi:10.1088/1748-9326/9/8/084004, 2014.

Pomeroy, J. W.: The cold regions hydrological model: a platform for basing process representation and model structure on physical evidence, Hydrol. Process., 21, 2650–2667, doi:10.1002/hyp, 2007.

Prein, A. F., Gobiet, A., Suklitsch, M., Truhetz, H., Awan, N. K., Keuler, K. and Georgievski, G.: Added value of convection permitting seasonal simulations, , 2655–2677, doi:10.1007/s00382-013-1744-6, 2013.

Prein, A. F., Langhans, W., Fosser, G., Ferrone, A., Ban, N., Goergen, K., Keller, M., Tölle, M., Gutjahr, O., Feser, F., Brisson, E., Kollet, S., Schmidli, J., Van Lipzig, N. P. M. and Leung, R.: A review on regional convection-permitting climate modeling: Demonstrations, prospects, and challenges, Rev. Geophys., 53(2), 323–361, doi:10.1002/2014RG000475, 2015.

Rasmussen, K. L., Prein, A. F., Rasmussen, R. M., Ikeda, K. and Liu, C.: Changes in the convective population and thermodynamic environments in convection-permitting regional climate simulations over the United States, Clim. Dyn., (0123456789), 1–26, doi:10.1007/s00382-017-4000-7, 2017.

Remenda VH, van der Kamp G, Cherry JA (1996) Use of vertical profiles of • 180 to constrain estimates of hydraulic conductivity in a thick, unfractured aquitard. 32:2979–2987

Shangguan W, Dai Y, Duan Q, et al (2014) Journal of Advances in Modeling Earth Systems. J Adv Model Earth Syst 6:249–263. doi: 10.1002/2013MS000293.Received

Sherwood, S. C., Bony, S. and Dufresne, J.: Spread in model climate sensitivity traced to atmospheric convective mixing, , doi:10.1038/nature12829, 2014.

Siebert, S., Burke, J., Faures, J. M., Frenken, K., Hoogeveen, J., Döll, P. and Portmann, F. T.: Groundwater use for irrigation - A global inventory, Hydrol. Earth Syst. Sci., 14(10), 1863–1880, doi:10.5194/hess-14-1863-2010, 2010.

Smerdon, B. D.: A synopsis of climate change effects on groundwater recharge, J. Hydrol., 555, 125–128, doi:10.1016/j.jhydrol.2017.09.047, 2017.

Statistics Canada: Quarterly Estimates of the Population of Canada, the Provinces and the Territories, 11-3, Catalogue 91-001, Ottawa, 1996

Taylor, R. G.: Ground water and climate change, , 3(November 2012), doi:10.1038/NCLIMATE1744, 2013.

Tremblay, L., Larocque, M., Anctil, F. and Rivard, C.: Teleconnections and interannual variability in Canadian groundwater levels, J. Hydrol., 410(3–4), 178–188, doi:10.1016/j.jhydrol.2011.09.013, 2011.

UNESCO: Groundwater Resources of the Wrold and Their Use, edited by I. Zektser and L. Everett, Paris., 2004.

Van Der Kamp G, Hayashi M (2009) Groundwater-wetland ecosystem interaction in the semiarid glaciated plains of North America. Hydrogeol J 17:203–214. doi: 10.1007/s10040-008-0367-1

Xue Y, Sellers PJ, Kinter JL, Shukla J (1991) A Simplified Biosphere Model for Global Climate Studies. J Clim 4:345–364. doi: 10.1175/1520-0442(1991)004<0345:ASBMFG>2.0.CO;2

Yang, Z. L., Niu, G. Y., Mitchell, K. E., Chen, F., Ek, M. B., Barlage, M., Longuevergne, L., Manning, K., Niyogi, D., Tewari, M. and Xia, Y.: The community Noah land surface model with multiparameterization options (Noah-MP): 2. Evaluation over global river basins, J. Geophys. Res. Atmos., 116(12), 1–16, doi:10.1029/2010JD015140, 2011.

755   Table and Figure

756

757   **Table 1.** Summary of the locations and aquifer type and soil type of the 33 selected wells.

Site Name/ Site No.	Lat	Lon	Elev	Aquifer type	Aquifer Lithology	Model Elevation	Model Soil type
Devon 0162	53.41	-113.76	700.0	Unconfined	Sand	697.366	Sandy loam
Hardisty 0143	52.67	-111.31	622.0	Unconfined	Gravel	633.079	Loam
Kirkpatrick Lake 0229	51.95	-111.44	744.5	Semi-confined	Sandstone	778.311	Sandy loam
Metiskow 0267	52.42	-110.60	677.5	Unconfined	Sand	679.516	Loamy sand
Wagner 0172	53.56	-113.82	670.0	Surficial	Sand	670.845	Silt loam
Narrow Lake 252	54.60	-113.63	640.0	Unconfined	Sand	701.0	Clay loam
Baildon 060	50.25	-105.50	590.184	Surficial	-	580.890	Sandy loam
Beauval	55.11	-107.74	434.3	Intertill	Sand	446.5	Sandy loam
Blucher	52.03	-106.20	521.061	Intertill	Sand/Gravel	523.217	Loam
Crater Lake	50.95	-102.46	524.158	Intertill	Sand/Gravel/Clay	522.767	Loam
Duck Lake	52.92	-106.23	502.920	Surficial	Sand	501.729	Loamy sand
Forget	49.70	-102.85	606.552	Surficial	Sand	605.915	Sandy loam
Garden Head	49.74	-108.52	899.160	Bedrock	Sand/Till	894.357	Clay loam
Nokomis	51.51	-105.06	516.267	Bedrock	Sand	511.767	Clay loam
Shaunavon	49.69	-108.50	896.040	Bedrock	Sand/Till	900.433	Clay loam
Simpson 13	51.45	-105.18	496.620	Surficial	Sand	493.313	Sandy loam
Simpson 14	51.457	-105.19	496.600	Surficial	Sand	493.313	Sandy loam
Yorkton 517	51.17	-102.50	513.643	Surficial	Sand/Gravel	511.181	Loam
Agrium 43	52.03	-107.01	500.229	Intertill	Sand	510.771	Loam
460120097591803	46.02	-97.98	401.177	Alluvial	Sand/Gravel	400.381	Sandy loam
461838097553402	46.31	-97.92	401.168	-	Sand/Gravel	404.719	Clay loam
462400097552502	46.39	-97.92	409.73	-	Sand/Gravel	407.405	Sandy loam
462633097163402	46.44	-97.27	325.52	Alluvial	Sand/Gravel	323.728	Sandy loam
463422097115602	46.57	-97.19	320.40	Alluvial	Sand/Gravel	314.167	Sandy loam
464540100222101	46.76	-100.37	524.91	-	Sand/Gravel	522.600	Clay loam
473841096153101	47.64	-96.25	351.77	Surficial	Sand/Gravel	344.180	Loamy sand
473945096202402	47.66	-96.34	327.78	Surficial	Sand/Gravel	328.129	Sandy loam
474135096203001	47.69	-96.34	325.97	Surficial	Sand/Gravel	327.764	Sandy loam
474436096140801	47.74	-96.23	341.90	Surficial	Sand/Gravel	336.210	Sandy loam
475224098443202	47.87	-98.74	451.33	-	Sand/Gravel	450.463	Sandy loam
481841097490301	48.31	-97.81	355.61	-	Sand/Gravel	359.568	Clay loam
482212099475801	48.37	-99.79	488.65	-	Sand/Gravel	488.022	Sandy loam
CRN Well WLN03	45.98	-95.20	410.7	Surficial	Sand/Gravel	411.4	Sandy loam

758

759 **Table 2.** Summary of mean and standard deviation (std) of WTD from 33 groundwater wells, from
760 observation records (OBS), default model (CTRL) and replacing with sand soil simulation (REP).
761 Bold texts indicate improvement in the REP than the CTRL run.
762

Site Name/Number	OBS_mean	CTRL_mean	REP_mean	OBS_std	CTRL_std	REP std
Devon 0162	-2.46	-2.69	**-2.38**	0.43	0.45	0.09
Hardisty 0143	-2.44	-8.91	**-6.88**	0.41	0.64	**0.36**
Kirkpatrick Lake 0229	-4.22	-4.03	-3.45	0.43	0.98	**0.22**
Metiskow 0267	-2.54	-5.39	**-4.43**	0.34	0.78	**0.55**
Narrow Lake 252	-2.31	-4.81	**-3.75**	0.28	0.60	0.51
Wagner 0172	-2.14	-8.06	**-2.70**	0.48	0.37	0.21
Baildon 060	-2.80	-3.29	**-3.20**	0.47	0.58	0.30
Beauval	-3.78	-4.85	**-4.20**	0.44	0.56	0.32
Blucher	-2.20	-4.24	**-2.16**	0.3	0.92	**0.26**
Crater Lake	-4.33	-3.97	-3.64	1.1	0.4	0.28
Duck Lake	-3.65	-3.69	-3.17	0.54	0.41	**0.62**
Forget	-2.28	-2.37	**-2.23**	0.33	0.17	0.19
Garden Head	-3.67	-4.85	**-3.77**	0.88	0.70	0.30
Nokomis	-1.04	-2.70	**-2.17**	0.23	0.55	**0.17**
Shaunavon	-1.62	-4.41	**-2.58**	0.42	0.69	0.20
Simpson 13	-4.82	-4.83	-3.02	0.31	0.91	**0.17**
Simpson 14	-2.03	-2.61	**-1.82**	0.34	0.18	**0.27**
Yorkton 517	-2.87	-3.97	**-1.98**	0.8	0.46	0.32
Agrium 43	-2.66	-3.75	**-3.38**	0.32	1.05	**0.36**
460120097591803	-1.44	-2.33	**-1.63**	0.56	0.24	**0.50**
461838097553402	-1.17	-2.32	**-1.68**	0.27	0.24	0.43
462400097552502	-4.9	-5.61	**-5.37**	0.29	0.09	**0.17**
462633097163402	-1.18	-1.49	**-1.02**	0.46	0.29	**0.54**
463422097115602	-1.36	-2.28	**-1.66**	0.34	0.23	0.49
464540100222101	-2.02	-3.64	**-2.78**	0.52	0.43	0.32
473841096153101	-0.77	-1.48	**-1.37**	0.24	0.18	0.51
473945096202402	-1.59	-1.58	-1.56	0.32	0.24	0.51
474135096203001	-0.72	-1.48	**-1.30**	0.33	0.25	0.54
474436096140801	-2.44	-2.29	-1.96	0.39	0.21	**0.40**
475224098443202	-4.52	-4.28	-5.31	0.75	0.52	0.34
481841097490301	-4.39	-4.24	-4.58	0.79	0.28	0.17
482212099475801	-2.13	-2.32	**-2.26**	0.24	0.20	0.17
CRN WLN 03	-2.04	-2.18	-1.88	0.24	0.18	0.43

763
764

765

766   (a)   (b)

767

768
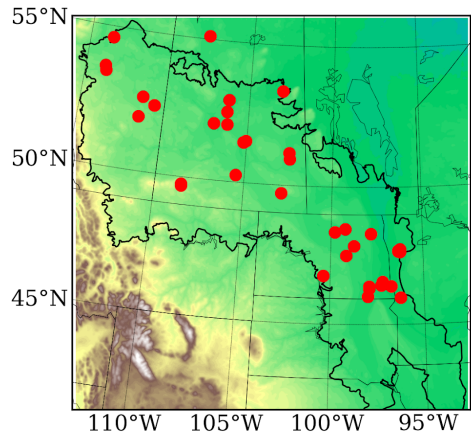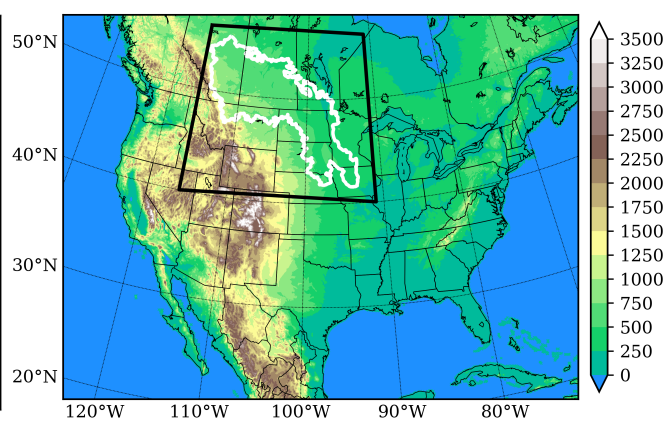
Fig. 1 (a) Topography of the Prairie Pothole Region (PPR; black outline) and groundwater wells (red dots); (b) Topography
of the WRF CONUS domain, the black box indicates the PPR domain.

771

772
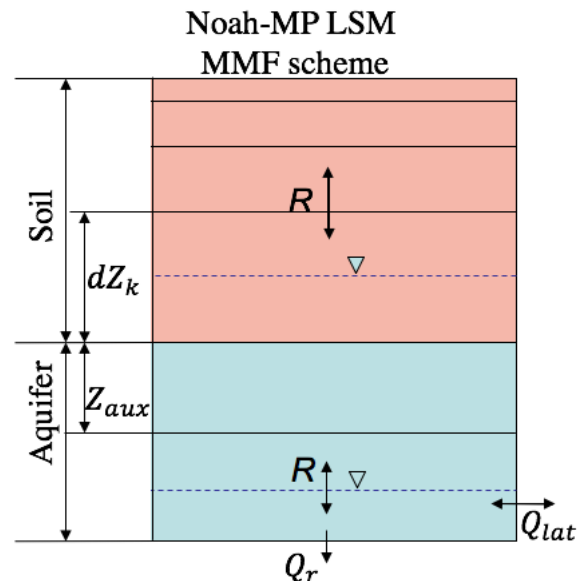
773

774 **Fig. 2** Structure of the Noah-MP LSM coupled with MMF groundwater scheme, the top 2-m soil of 4 layers whose thicknesses
775 are $0.1, 0.3, 0.6$ and 1.0 m. An unconfined aquifer is added below the 2-m boundary, including an auxiliary layer and the saturated
776 aquifer. Positive flux of R denotes downward flow. Two water tables are shown, one within the 2-m soil and one below,
777 indicating that the model is capable to deal with both shallow and deep water table.
778
779

780
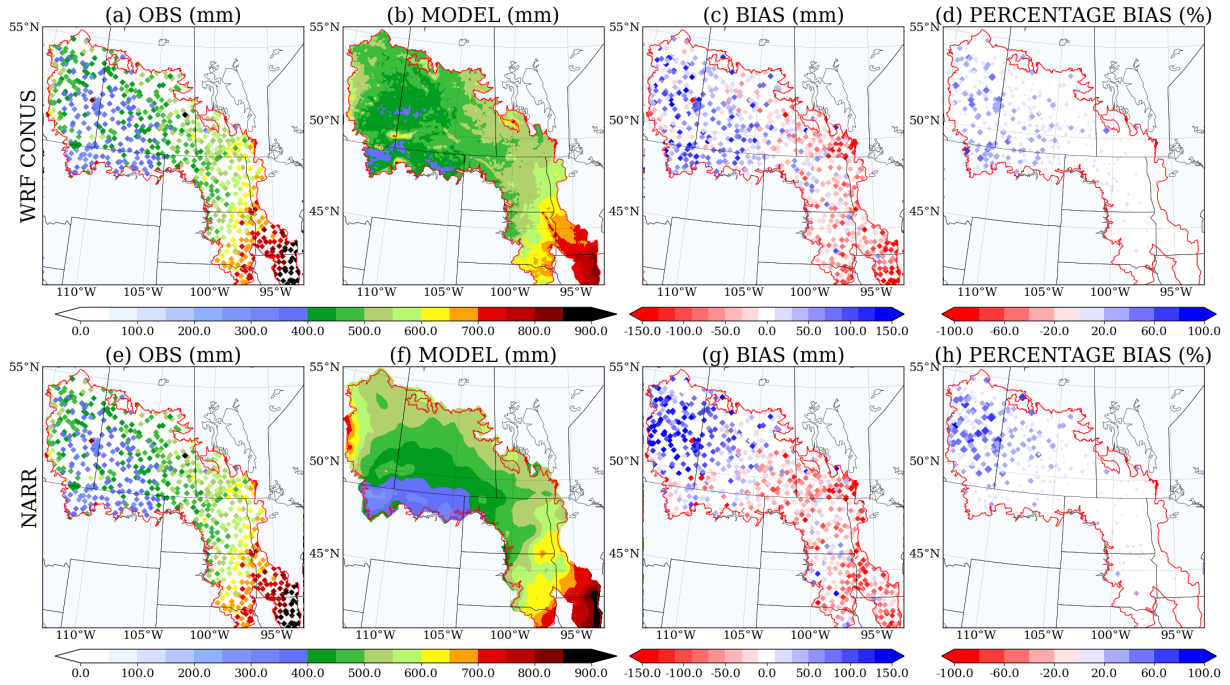
781
782
783 **Fig. 3** Evaluation of the annual precipitation from two model products (b, f), WRF CONUS and NARR against
784 rain gauge observation (a, e), their bias (c, g) and percentage bias (d, h).
785
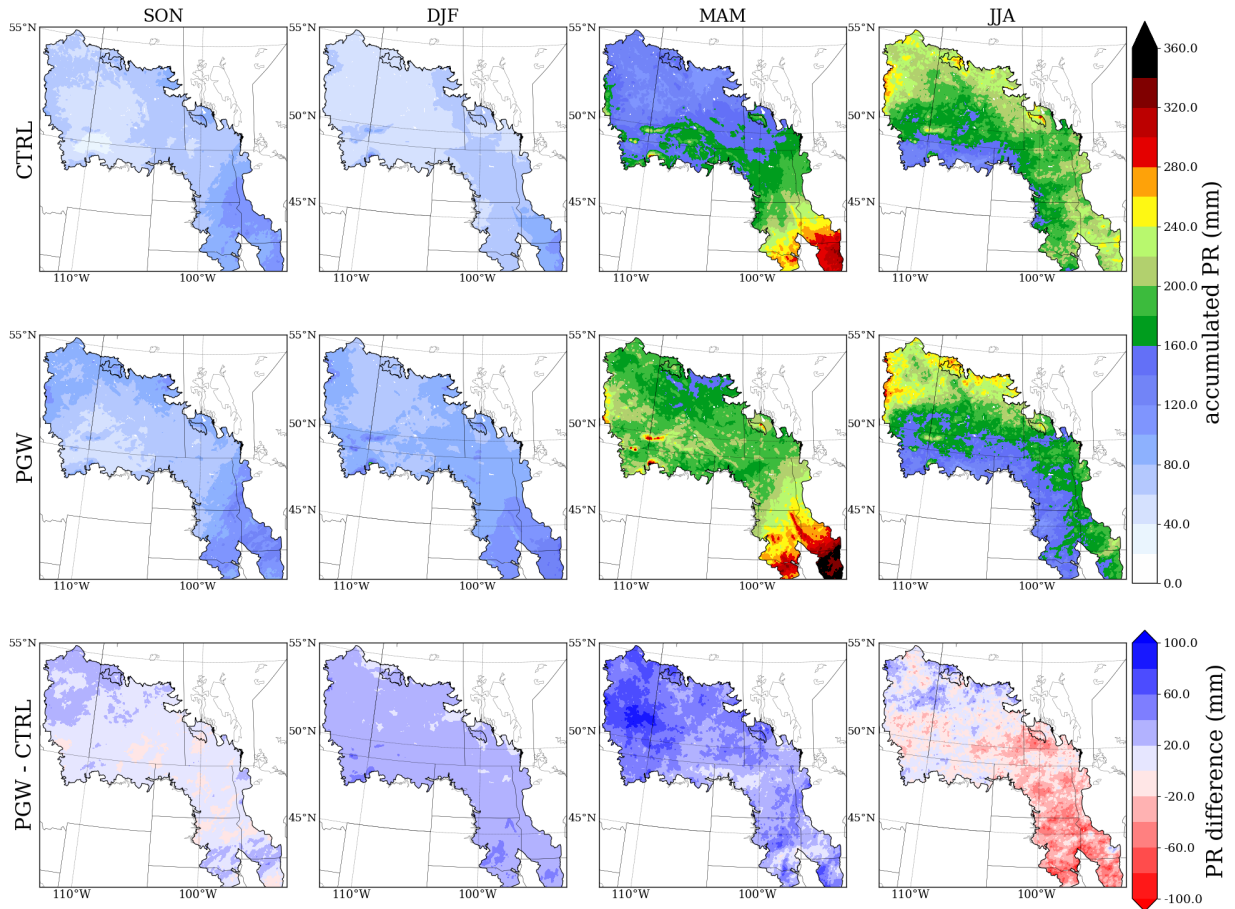
786
787 **Fig. 4** Seasonal Accumulated precipitation from current climate (CTRL, top), future climate (PGW, middle) and
788 projected change (PGW-CTRL, bottom) in forcing data.
789
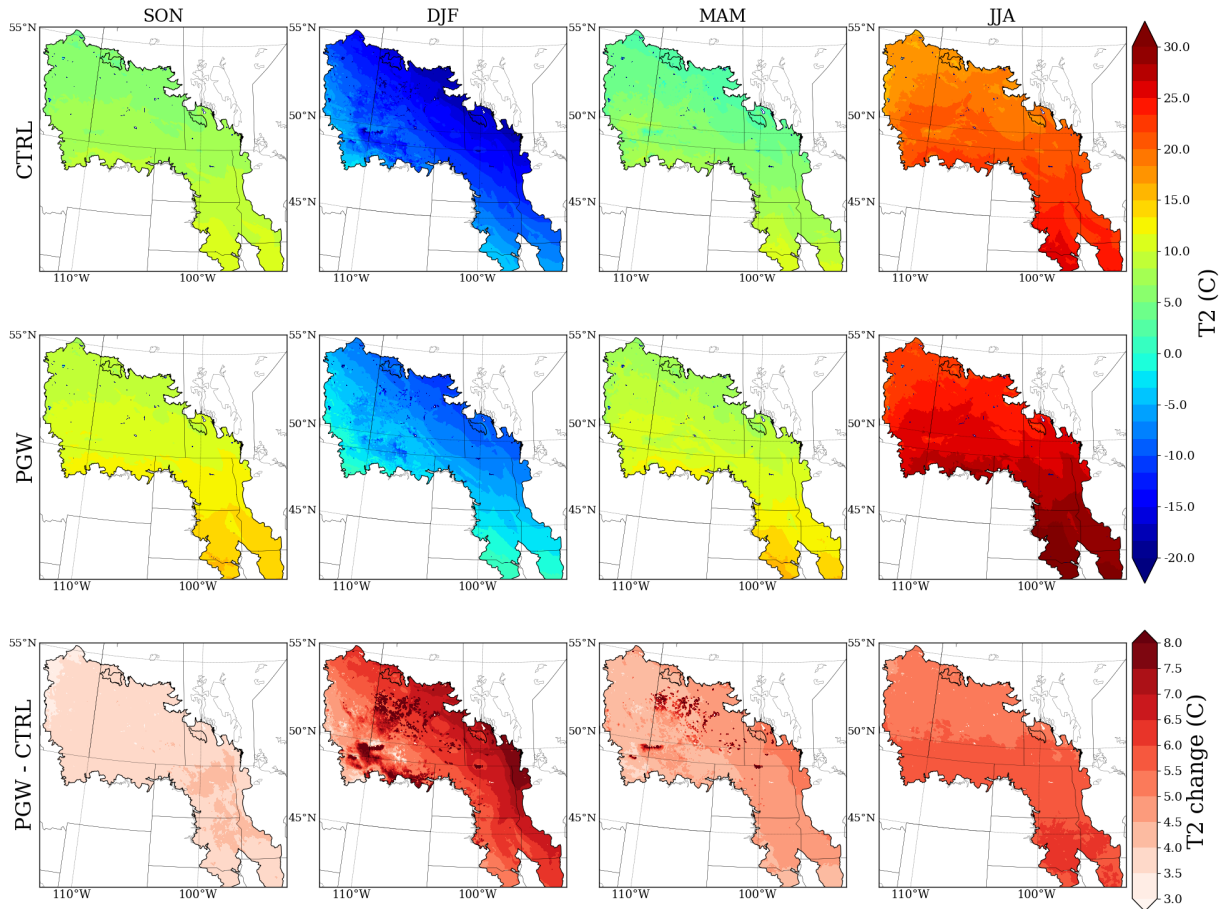
790
791 **Fig. 5** Seasonal temperatures from current climate (CTRL, top), future climate (PGW, middle) and projected
792 change (PGW-CTRL, bottom) in forcing data.
793

794
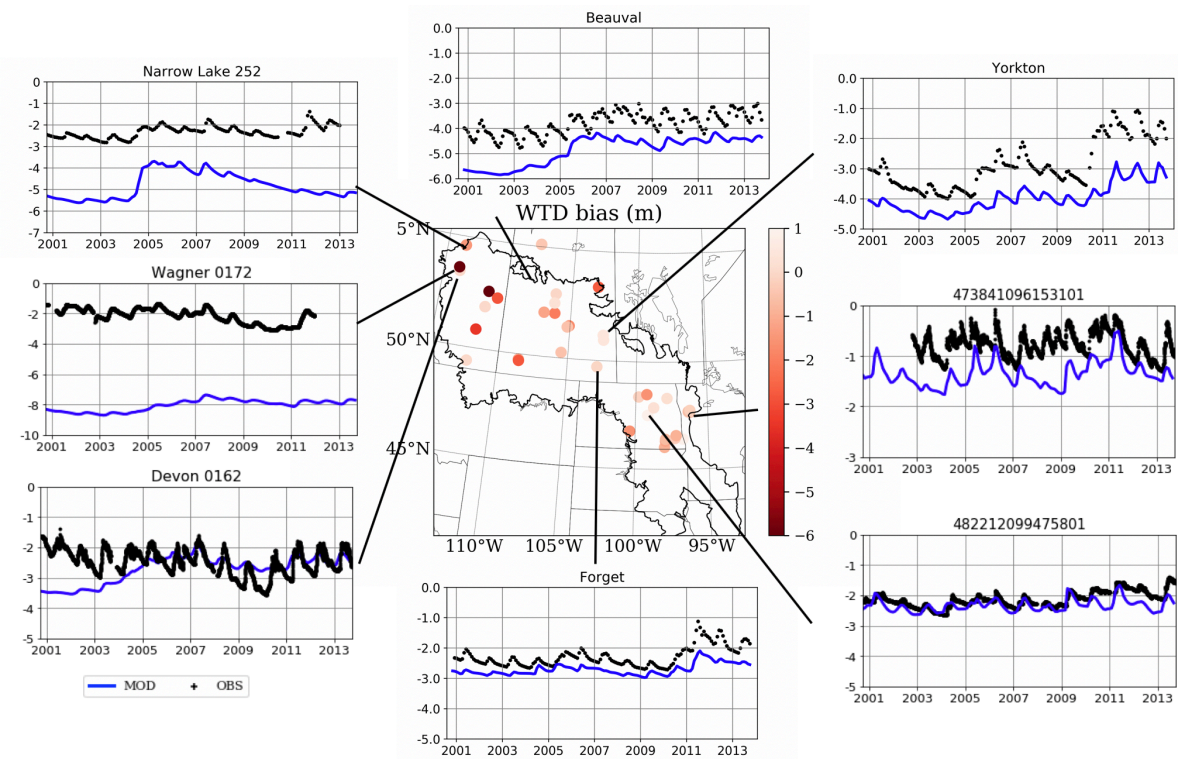
795
796
797 **Fig. 6.** WTD (m) bias from CTRL simulation and timeseries from 8 groundwater wells in PPR (black for observation and
798 blue for CTRL model simulation). See Table 2 CTRL column for the model statistics and supplemental materials for complete
799 timeseries from 33 wells.
800
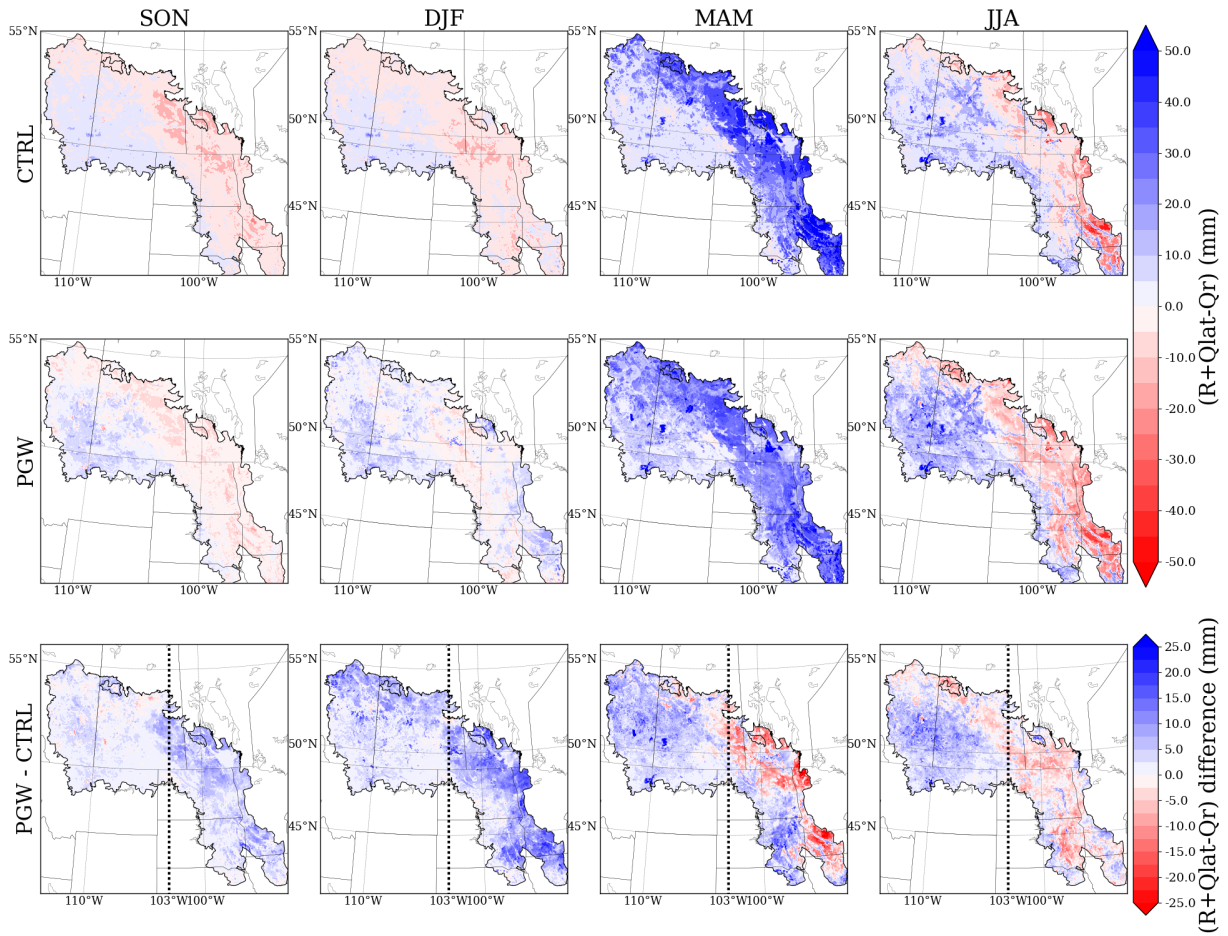
801
802 **Fig. 7** Seasonal accumulated total groundwater fluxes ($R+Q_{lat}-Q_r$) for current climate (CTRL, top), future
803 climate (PGW, middle) and projected change (PGW-CTRL, bottom) in forcing data. Black dashed lines in PGW-
804 CTRL separate the PPR into eastern and western halves.
805

storage change: 1.763 mm
recharge change: 4.152 mm
river flux change: 2.260 mm
lateral flux change: -0.001 mm

Fig. 8 Water budget analysis in the **eastern PPR** in (a) CTRL, (b) PGW and (c) PGW – CTRL. Water budget terms include: (1) *PR & ET*, (2) surface snow, surface runoff and underground runoff (*SNOW*, *SFCRUN*, and *UDGRUN*), (3) change of soil moisture storage (soil water, soil ice and total soil moisture, ΔSMC) and (4) groundwater fluxes and the change of groundwater storage (R, Q_{lat}, Q_r, ΔS_g). The annual mean soil moisture change (PGW-CTRL) is shown with black dashed line in (3). The Residual term is defined as $Res = (R+Q_{lat}-Q_r)-\Delta S_g$ in (4). Note that in (a) and (b) the accumulated fluxes and change in storage are shown in lines, whereas in (c) the difference in (PGW-CTRL) is shown for each individual month in bars.

storage change: 5.390 mm
recharge change: 10.727 mm
river flux change: 5.207 mm
lateral flux change: 0.000 mm

Fig. 9 Same as Fig. 8. Water budget analysis in the **western PPR**: in (a) CTRL, (b) PGW and (c) PGW – CTRL. Water budget terms include: (1) *PR & ET*, (2) surface snow, surface runoff and underground runoff (*SNOW, SFCRUN, and UDGRUN*), (3) change of soil moisture storage (soil water, soil ice and total soil moisture, ΔSMC) and (4) groundwater fluxes and the change of groundwater storage ($R, Q_{lat}, Q_r, \Delta S_g$). The annual mean soil moisture change (PGW-CTRL) is shown with black dashed line in (3). The Residual term is defined as $Res = (R+Q_{lat}-Q_r)-\Delta S_g$ in (4). Note that in (a) and (b) the accumulated fluxes and change in storage are shown in lines, whereas in (c) the difference in (PGW-CTRL) is shown for each individual month in bars.
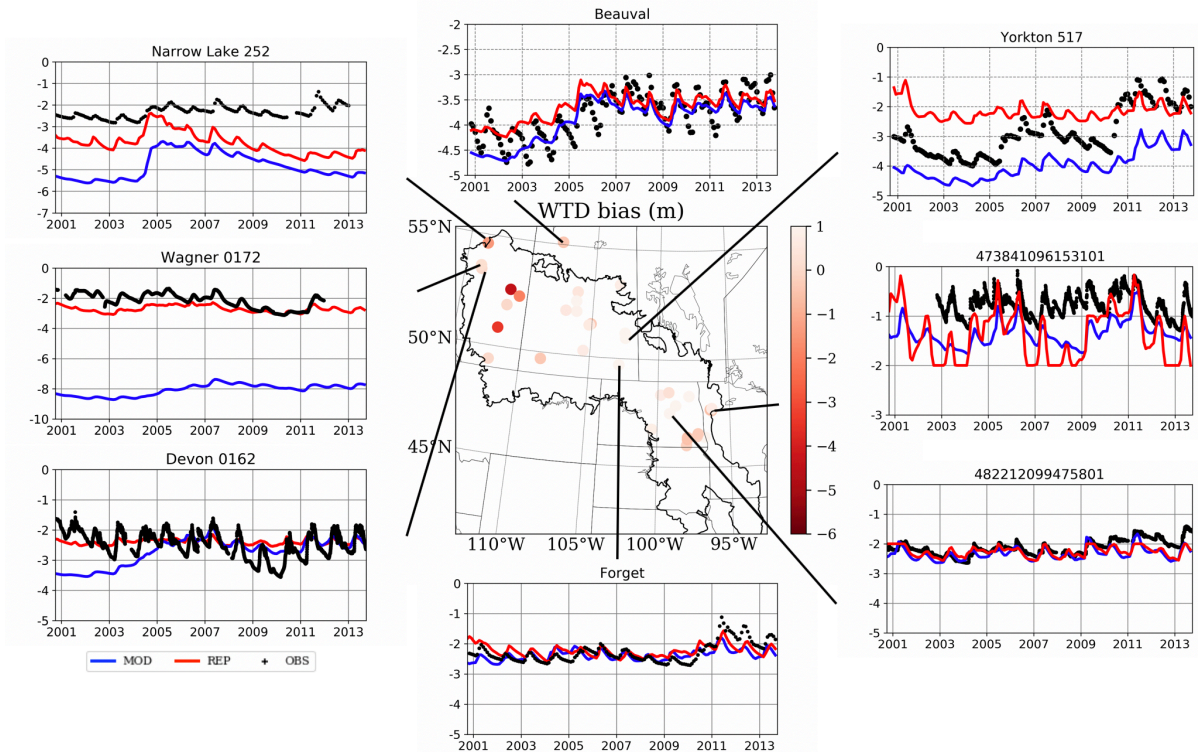
827
828 **Fig. 10** Same as Fig. 6, WTD (m) bias from CTRL simulation and timeseries from 8 groundwater wells in PPR (black for
829 observation and blue for CTRL model simulation, and red for the replacing soil type simulation). REP is the additional
830 simulation by replacing the default soil type in the model with sandy soil type.
831
832
833